ADVANCES IN ATMOSPHERIC SCIENCES, VOL. 39, DECEMBER 2022, 2024–2039

• **Original Paper** •

Application of a Neural Network to Store and Compute the Optical Properties of Non-Spherical Particles※

Jinhe YU[1], Lei BI[*1], Wei HAN[*2,3], and Xiaoye ZHANG[4]

[1]*Key Laboratory of Geoscience Big Data and Deep Resource of Zhejiang Province, School of Earth Sciences, Zhejiang University, Hangzhou* 310027, *China*

[2]*Center for Earth System Modeling and Prediction, China Meteorological Administration, Beijing* 100081, *China*

[3]*Numerical Weather Prediction Center, China Meteorological Administration, Beijing* 100081, *China*

[4]*Key Laboratory of Atmospheric Chemistry of China Meteorological Administration, Institute of Atmospheric Composition, Chinese Academy of Meteorological Sciences, Beijing* 100081, *China*

(Received 22 September 2021; revised 17 November 2021; accepted 23 November 2021)

ABSTRACT

Radiative transfer simulations and remote sensing studies fundamentally require accurate and efficient computation of the optical properties of non-spherical particles. This paper proposes a deep learning (DL) scheme in conjunction with an optical property database to achieve this goal. Deep neural network (DNN) architectures were obtained from a dataset of the optical properties of super-spheroids with extensive shape parameters, size parameters, and refractive indices. The dataset was computed through the invariant imbedding *T*-matrix method. Four separate DNN architectures were created to compute the extinction efficiency factor, single-scattering albedo, asymmetry factor, and phase matrix. The criterion for designing these neural networks was the achievement of the highest prediction accuracy with minimal DNN parameters. The numerical results demonstrate that the determination coefficients are greater than 0.999 between the prediction values from the neural networks and the truth values from the database, which indicates that the DNN can reproduce the optical properties in the dataset with high accuracy. In addition, the DNN model can robustly predict the optical properties of particles with high accuracy for shape parameters or refractive indices that are unavailable in the database. Importantly, the ratio of the database size (~127 GB) to that of the DNN parameters (~20 MB) is approximately 6810, implying that the DNN model can be treated as a highly compressed database that can be used as an alternative to the original database for real-time computing of the optical properties of non-spherical particles in radiative transfer and atmospheric models.

Key words: non-spherical particles, light scattering, super-spheroid model, deep learning, neural network

Citation: Yu, J. H., L. Bi, W. Han, and X. Y. Zhang, 2022: Application of a neural network to store and compute the optical properties of non-spherical particles. *Adv. Atmos. Sci.*, **39**(12), 2024–2039, https://doi.org/10.1007/s00376-021-1375-5.

Article Highlights:

- An optical property dataset computed through the T-matrix method can be highly compressed using an optimized deep neural network.
- The optical properties of super-spheroid models can be accurately and efficiently computed through a neural network.
- The neural network can be used instead of a conventional look-up table in atmospheric radiative transfer and related atmospheric models.

1. Introduction

Aerosol particles suspended in the atmosphere are important components in the earth-atmosphere system and play a significant role in atmospheric physics and radiation processes (Charlson et al., 1992; Satheesh and Moorthy, 2005; Kok et al., 2017). Aerosols affect the climate by reflecting and absorbing solar radiation (Tegen et al., 1996; Myhre et al., 2013) and exert an enormous influence on precipitation by altering the microphysics, life cycles, and radiative processes of clouds (Rosenfeld, 2000; Rosenfeld et al., 2008; Li et al., 2011). Moreover, aerosols can cause environmental

※ This paper is a contribution to the special issue on Cloud–Aerosol–Radiation–Precipitation Interaction: Progress and Challenges.

* Corresponding authors: Lei BI, Wei HAN
Emails: bilei@zju.edu.cn, hanwei@cma.gov.cn

pollution, such as haze (Zhang, 2010; Morman and Plumlee, 2013; Zhang et al., 2015; Wang et al., 2016). Therefore, the physical and chemical characteristics of aerosols, including their radiative, weather, and climate effects, have always been important issues in atmospheric science (IPCC, 2013).

To improve the understanding of the interaction between aerosols, radiation, and the atmosphere, accurate quantification of the optical scattering and absorption characteristics of aerosols is necessary, including the extinction coefficient, single-scattering albedo, symmetry factor, and phase matrix (Sokolik et al., 1993; Heintzenberg et al., 1997; Dubovik et al., 2002). Specifically, the accurate simulation of single and multiple scattering characteristics of aerosols is also a key problem in forward radiative transfer and inversion remote sensing algorithms related to aerosols (King et al., 1999; Dubovik et al., 2008, 2019). Aerosols have diverse shapes, and countless variables are required to describe their physical characteristics and diversity accurately. However, to facilitate research, a simplified parameterization scheme with constrained degrees of freedom has to be adopted.

Conventional methods mostly use a spherical approximation or spheroidal approximation. Spherical approximation problems can be solved exactly by the Lorenz-Mie theory (Bohren and Huffman, 1983). However, this method has proven to be a great source of error in the inversion of aerosol optical thickness and estimation of climatic effects involving non-spherical aerosols (Mishchenko et al., 1995, 2003; Zhao et al., 2003; Kahnert and Kylling, 2004; Kahnert et al., 2007). The spheroid approximation yields better performance but requires further improvements (Kahnert et al., 2002; Dubovik et al., 2006; Nousiainen et al., 2011). The optical properties of aerosols can also be computed using complex aerosol models that capture the detailed morphological features of sampled aerosols (Kahnert et al., 2014). Still, it is not trivial to examine the general representativeness of such models, nor is it efficient to apply them broadly.

Our team has extensively examined the super-spheroid model in the past few years. Compared with the spheroid model, it has greater freedom in shape-changing. Thus far, it has been applied to the studies of optical properties of dust and mixed-dust aerosols (Lin et al., 2018; Tang et al., 2019), as well as the study of the optical properties and radiative forcing of sea salt (Bi et al., 2018; Wang et al., 2019). The use of the super-spheroidal model is also quite promising for computing the optical properties of ice crystals (Sun et al., 2021). This new parameterization enables the continuous simulation of the shape of particles and lays a foundation for establishing a database of the optical properties of particles.

Compared to the spherical approximation, calculating the optical properties of non-spherical particles is much slower. Some advanced electromagnetic scattering computing techniques have been used, such as the discrete dipole approximation method (Draine and Flatau, 1994; Yurkin and Hoekstra, 2011), the finite-difference time-domain method (Yang and Liou, 1996b; Yee, 1966), the pseudo-spectral time-domain method (Liu, 1997; Liu et al., 2012), the boundary element method (Groth et al., 2015), the improved geometrical optics method (IGOM) (Yang and Liou, 1996a; Yang et al., 2007; Bi et al., 2009), and the invariant imbedding *T*-matrix method (IITM) (Johnson, 1988; Bi et al., 2013a, b; Bi and Yang, 2014). Nevertheless, large-scale computation is quite time-consuming, and it is unfeasible to achieve real-time computing in radiative transfer models. Therefore, the conventional way of solving this problem is to establish a database of non-spherical particles (Yang et al., 2013; Bi and Yang, 2017; Saito et al., 2021).

A database of optical properties can be designed as a look-up table (LUT) with data corresponding to different particle habits that have been pre-calculated. When it is time to call the optical properties of certain particles, it is unnecessary to wait for the results of the calculation, and the exact value or a near-optimal interpolated solution can be directly obtained from the LUT. However, with the increase of parameters, the database becomes increasingly massive and occupies a large amount of computer storage space, limiting its convenience for various applications.

In recent years, numerous deep learning (DL) approaches have been widely explored, especially in the field of identifications and optimizations (Hinton and Salakhutdinov, 2006; Bengio, 2009; LeCun et al., 2015), further noting that DL is a several decades-old technique in statistics and computer science, which has since gained popularity due to new aspects in large-scale commercial applications in software companies (Silver et al., 2016; Shrivastava et al., 2021). These state-of-the-art methods are not only influential in the field of computer sciences (Hinton et al., 2012; Krizhevsky et al., 2012; Oquab et al., 2014) but are also bringing about new research perspectives in conventional science and engineering fields. For example, Chen et al. (2016) extracted in-depth features from hyperspectral images that are non-linear, discriminant, and invariant by using a convolutional neural network. Ham et al. (2019) proposed a DL method to accurately predict the El Niño/Southern Oscillation (ENSO), known to be associated with regional climate extremes and ecosystem impacts. Di Noia and Hasekamp (2018) reviewed the theoretical basis of applying machine learning algorithms to the field of cloud and aerosol remote sensing and discussed their advantages and disadvantages in comparison with conventional methods.

The DL approach has flourished largely because of its ability to extract physical information from vast amounts of data. Therefore, it is theoretically possible to learn the optical properties of particles using a deep neural network (DNN) and then predict them, as opposed to solving Maxwell's equations. In addition, the optical property information can be stored as network parameters throughout the training process, which could replace an enormous database by saving a small DNN model instead.

In this paper, we propose a suitable DL scheme to compute the optical properties of non-spherical particles, which

can simultaneously overcome the speed and portability problem of conventional methods and facilitate the use of a non-spherical model for practical applications. In section 2, we describe the super-spheroidal model and the DL approach. We present the details of the DNN architecture implementation in section 3.1. The performance of the DNN models and the feasibility of the DL schemes are discussed in section 3.2 to include representative examples. The conclusions are summarized in section 4.

2. Methodology and definitions

2.1. *Parameterization*

We used the super-spheroid as a simplified model to mimic atmospheric particles because it has been demonstrated as a promising model for the optical properties of dust and sea salt aerosols (Bi et al., 2018; Lin et al., 2018), although realistic particle shapes could be much more complex than super-spheroids. The super-spheroidal equation is defined as follows (Barr, 1981; Wriedt, 2002):

$$\left(\frac{x}{a}\right)^{\frac{2}{n}}+\left(\frac{y}{a}\right)^{\frac{2}{n}}+\left(\frac{z}{c}\right)^{\frac{2}{n}}=1\,, \tag{1}$$

where a and c are the length of the horizontal and vertical axes in a Cartesian coordinate system, and n is the roundness parameter, which determines whether a particle is sharp or smooth. This model can generate a large number of particles by changing the aspect ratio and roundness parameter. Figure 1 demonstrates twenty-five typical shapes of super-spheroids. Importantly, the shape variation is continuous so that the shape parameters can be directly used as training parameters in a DNN.

The optical properties include the extinction efficiency factor Q_{ext}, the single scattering albedo SSA, the asymmetry factor g, and the phase matrix element P_{ij}. The extinction efficiency factor Q_{ext} can then be defined as:

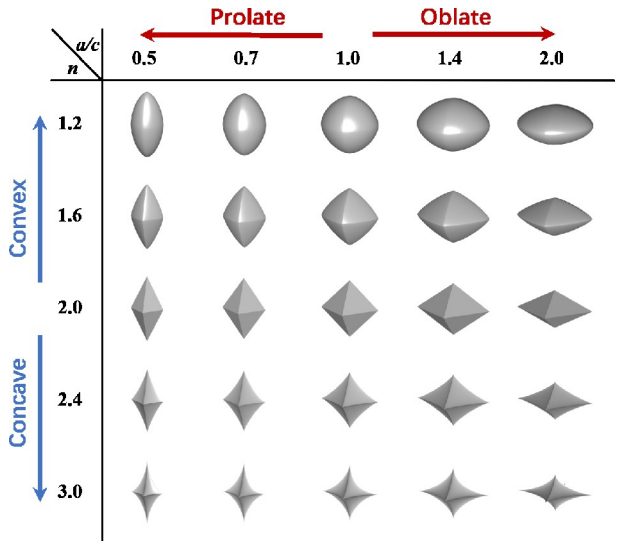

Fig. 1. Twenty-five representative super-spheroid shapes including oblate ($a/c > 1.0$), prolate ($a/c < 1.0$), concave ($n > 2.0$), and convex particles ($n < 2.0$).

$$Q_{\text{ext}}=\frac{C_{\text{ext}}}{A_{\text{proj}}}\,, \tag{2}$$

$$A_{\text{proj}}=\pi(\text{xsize}\cdot\text{factor})^2\,, \tag{3}$$

where C_{ext} is the extinction cross-section, A_{proj} is the projected cross-sectional area of the super-spheroidal particle, xsize represents the size parameter of the particle, and factor is determined by the aspect ratio a/c and the roundness parameter n, which are computed by a Monte-Carlo ray-tracing technique. Specifically, for each particle orientation, the projected area was determined by counting the proportion of "photons" falling within the projected shadow. The averaged projected area was obtained by taking the average of projected areas associated with several orientations. SSA is defined as:

$$\text{SSA}=\frac{C_{\text{sca}}}{C_{\text{ext}}}\,, \tag{4}$$

in which C_{sca} is the scattering cross-section. The asymmetry factor g represents a measure of the angular distribution of the scattering intensity. The scattering matrix P_{ij} determines the relationship between the Stokes vectors of the incident beam $(\boldsymbol{I}_0,\boldsymbol{Q}_0,\boldsymbol{U}_0,\boldsymbol{V}_0)$ and that of the scattered beam $(\boldsymbol{I}_{\text{s}},\boldsymbol{Q}_{\text{s}},\boldsymbol{U}_{\text{s}},\boldsymbol{V}_{\text{s}})$, which is given by (Bohren and Huffman, 1983):

$$\begin{bmatrix}\boldsymbol{I}_{\text{s}}\\ \boldsymbol{Q}_{\text{s}}\\ \boldsymbol{U}_{\text{s}}\\ \boldsymbol{V}_{\text{s}}\end{bmatrix}=\left(\frac{1}{kR}\right)^2\begin{bmatrix}P_{11}(\theta) & P_{12}(\theta) & 0 & 0\\ P_{21}(\theta) & P_{22}(\theta) & 0 & 0\\ 0 & 0 & P_{33}(\theta) & P_{34}(\theta)\\ 0 & 0 & P_{43}(\theta) & P_{44}(\theta)\end{bmatrix}\begin{bmatrix}\boldsymbol{I}_0\\ \boldsymbol{Q}_0\\ \boldsymbol{U}_0\\ \boldsymbol{V}_0\end{bmatrix}, \tag{5}$$

where θ is the scattering angle, ranging from 0° to 180°, k is the corrected wave number, and R is the distance between the scatter and the detector. The intensity of the light beam is given by $\boldsymbol{I}$, while $\boldsymbol{Q}$, $\boldsymbol{U}$, and $\boldsymbol{V}$ describe the linear and circular polarization of the beam. For randomly oriented super-spheroids (note, the particles have a plane of symmetry), $P_{12}=P_{21}$, and $P_{34}=-P_{43}$ (Van De Hulst, 1981; Mishchenko and Yurkin, 2017).

2.2. *Deep learning*

Deep learning is one of the latest trends in Machine Learning (ML) and Artificial Intelligence (AI) research. A deep neural network has good self-adaptation capabilities. It is trained through a batch of corresponding input and output data, allowing for the intrinsic relationship between the input and output to be resolved in the final form of a complex non-linear system function (Schmidhuber, 2017). In most situations, a DNN architecture is a multi-level, non-linear repetition of a simple neuron that obtains highly intricate functions

from the input. This kind of network is composed of simple neurons in a complex system that processes information through the relationship between the internal nodes. In this study, the procedure mentioned above in the context of artificial neural networks is essentially a non-linear statistical regression. The hidden layers containing some neurons constitute a deep neural network. The output results $\boldsymbol{o}^{(l)}$ of neurons in the layer l was calculated from the output of the previous layers $\boldsymbol{o}^{(l-1)}$:

$$\boldsymbol{o}^{(l)} = \varphi\left(\sum_{j=1}^{N^{(l-1)}} \boldsymbol{w}_{i,j}^{(l)} \boldsymbol{o}_j^{(l-1)} + \boldsymbol{b}_i^{(l)}\right), \tag{6}$$

where φ is a non-linear activation function, $N^{(l-1)}$ is the sum of nodes in layer $l-1$, $\boldsymbol{w}_{i,j}^{(l)}$ and $\boldsymbol{b}_i^{(l)}$ are the weights and biases in layer l, respectively. The node i in layer l must satisfy the relation $1 \leqslant i \leqslant N^{(l)}$.

The parametric scheme mentioned in section 2.1 makes a DL scheme feasible. All of the parameters (shape parameters, refractive indices, and size parameters) are continuous and smooth. Compared to particle shape models without continuous particle parameters, super-spheroid models in conjunction with DL schemes are very suitable for establishing relationships between the input (particle shapes, refractive indices, and particle sizes) and the output (the optical properties). Once the relationships are established through DL schemes, the optical properties of particles in the atmosphere can be directly obtained by the neural networks.

The neural network method is an optimal choice to compress the database. In principle, if we want to preserve a neural network, we can do it by saving the weights and biases of the neurons in each of the hidden layers. As the number of parameters increases, so does the storage size of the model file. Then, we can just use the trained and preserved DNN models to predict the optical properties of specific particles. To use the DNN model instead of the original database, we must achieve the following goals: (1) obtain a file size of a saved DNN model that is much smaller than that of the database size, and (2) design a model that can predict particle properties with high accuracy. The value of the learning rate in the Adam algorithm and the patience parameter of early stopping should be tuned in the training procedure (details in section 2.4). In addition, various weight initialization methods and batch sizes of input data also need to be adjusted.

2.3. *Dataset*

The database chosen in this study contains abundant non-spherical particles based on the super-spheroidal model. The optical properties of super-spheroids are computed by using the IITM for all combinations of shape parameters, the complex refractive index, and the size parameter. The aspect ratio a/c ranges from 0.5 to 2.0, and the roundness parameter n ranges from 1.2 to 3.0. A total of 110 super-spheroid shapes are considered.

The refractive index is complex, and its real part m_r ranges from 1.30 to 1.80, while the imaginary part m_i ranges from 10^{-7} to 0.1. The dataset is computed using 11 real parts and 9 imaginary parts (99 complex refractive indices in all). In the single-scattering computation, the size parameter xsize ranges from 0.1 to 50 with 180 discrete values, and the scattering angle θ ranges from 0° to 180° with 721 discrete values. For convenience, the parameters of the database are explicitly given in Table 1.

The optical properties include the extinction efficiency factor Q_ext, single scattering albedo SSA, asymmetry factor g, and all phase matrix elements P_{ij}. The results in the database computed from the IITM are used as truth values when training and testing the DNN models. The total amount of data in the set is 1 960 200 for the optical properties Q_ext, SSA, and g. For the phase matrix element P_{ij}, the dataset contains 1 413 304 200 combinations because the scattering angle θ is involved.

The optical data of non-spherical particles can be obtained immediately from the database, so it is unnecessary to solve Maxwell's equations, and computation speed is no longer a problem. However, as more and more particles or parameters are considered, the size of the database increases substantially. The parameters given in Table 1 would take up almost 133 377 877 kilobytes (~127 GB) of hard disk storage space for saving the data in ASCII format. Thus, it is inconvenient to apply the dataset in scientific research. In addition, if the shape parameters or refractive indices are

Table 1. Super-spheroid optical properties database. The real part of the refractive index m_r ranges from 1.30 to 1.80, while the imaginary part m_i ranges from 10^{-7} to 0.1. The aspect ratio a/c ranges from 0.5 to 2.0, and the roundness parameter n ranges from 1.2 to 3.0. The size parameter xsize ranges from 0.1 to 50, and the scattering angle θ ranges from 0° to 180°. The optical properties include the extinction efficiency factor Q_ext, single scattering albedo SSA, asymmetry factor g, and all phase matrix elements P_{ij}.

Parameters	Values	Optical Properties
Real Part of the Refractive Index m_r	1.30, 1.35, 1.40, 1.45, 1.50, 1.55, 1.60, 1.65, 1.70, 1.75, 1.80	Q_ext, SSA, g, P_{11}, P_{12}, P_{22}, P_{33}, P_{43}, and P_{44}
Imaginary Part of the Refractive Index m_i	10^{-7}, 10^{-6}, 10^{-5}, 0.0001, 0.001, 0.005, 0.01, 0.05, 0.1	
Aspect Ratio a/c	0.5, 0.6, 0.7, 0.8, 0.9, 1.0, 1.2, 1.4, 1.6, 1.8, 2.0	
Roundness n	1.2, 1.4, 1.6, 1.8, 2.0, 2.2, 2.4, 2.6, 2.8, 3.0	
Size Parameter xsize	0.1, 0.2, 0.3, …, 9.8, 9.9, 10 (step = 0.1); 10.2, 10.4, 10.6, …, 19.6, 19.8, 20 (step = 0.2); 21, 22, 23, …, 48, 49, 50 (step = 1);	
Scattering Angle θ(°)	0, 0.25, 0.5, 0.75, 1.0, 1.25, 1.5, 1.75, 2.0, 2.25, 2.5, 2.75, 3… 179, 179.25, 179.5, 179.75, 180 (step = 0.25)	

unavailable, we have to read the data from the database and then perform necessary interpolations.

2.4. *DNN architecture*

DNN Models are used to predict the extinction efficiency factor Q_{ext}, single scattering albedo SSA, asymmetry factor g, and phase matrix element P_{ij}. These models consist of several fully connected layers. The input layer has five inputs (m_{r}, m_{i}, a/c, n, xsize) for the Q_{ext}, SSA, and g and six inputs (m_{r}, m_{i}, a/c, n, xsize, θ) for the phase matrix elements P_{ij}.

The number of hidden layers and neurons varies for different optical properties. For example, for the extinction efficiency (Q_{ext}), five layers were designed. For convenience, the number of neuron nodes in each layer was included in parenthesis. For example, (Q_{ext}, 128) indicates that 128 neuron nodes in this layer were used for the prediction of Q_{ext}. Based on several tests (see section 3.1), we found that accurate prediction of SSA, g, and P_{ij} requires five, six, and seven layers, respectively. Among the nodes of hidden layers, every activation function was a rectified linear unit (ReLU) function, namely, $f(x) = \max(0, x)$. The chosen activation functions could build a sparse neural network and prevent over-fitting (Glorot et al., 2011). Moreover, a higher computational efficiency was achieved because no complex processes, such as exponential calculations, were involved in the ReLU function. However, we applied a linear mapping on the last layer instead of the ReLU function.

The networks were trained with the Adam algorithm, a stochastic gradient descent method based on an adaptive estimation of first-order and second-order moments (Kingma and Ba, 2015). The initial learning rate was set to 0.001, the exponential decay rates for the 1st- and 2nd-moment estimates were set to 0.9 and 0.999, respectively, and the epsilon parameter (a constant for controlling the numerical stability) was set to 10^{-7}. All weighting coefficients were initialized by the Glorot uniform initializer (Glorot and Bengio, 2010).

We implemented the DNN networks using the Keras API running on the TensorFlow2 ML platform (Abadi et al., 2016). The key tool is the parallel computing framework CUDA, which makes the training process efficient. The calculations were performed on an NVIDIA GeForce RTX 3070 GPU with 16 GB of memory. We saved the trained DNN model parameters in HDF5 file format. The optimal weight matrices (kernel) and bias vectors corresponding to each layer were saved in these files.

All data were split into a training set, a validation set, and a test set. The training set is used to fit the samples and change parameters between the adjacent units. The validation set is used to tune the hyperparameters of the models, save the optimal parameters of nodes in every epoch, and determine an early stopping point when the monitored metric stops improving. The test set is only used to evaluate the error and accuracy of the resulting model at the end. However, the amount of data in each set varies among different evaluation schemes.

We have designed three schemes for specific purposes (the details are in section 3). We used 70% of the data for training, 10% for validation, and 20% for testing. We selected 100 000 points or specific particles from the test set to verify the different targets. Before training, all input parameters were normalized to between 0 and 1.

To quantify the accuracy of the DNN predicted results, we used the root mean square error (RMSE) as a regression metric, which is defined as follows:

$$\text{RMSE} = \sqrt{\frac{1}{M}\sum_{i=1}^{M}(y_i - f_i)^2}\,, \tag{7}$$

where, y_i and f_i represent the i-th true value and the predicted value in the data samples, respectively, and M is the sample size. Once the validation loss decreases, the whole model is saved after every epoch. Thus, the model or weights can be loaded afterward to continue the training from the saved state. Training can be stopped early when the loss has stopped decreasing. We set the patience parameter to 20, which means that the training process is stopped if the validation loss does not decrease after 20 epochs. The patience parameter is also a sensible choice to avoid overfitting.

3. Results

3.1. *Optimized DNN models*

To achieve maximum compression for the database, we designed several DNN models, which resulted in different file sizes. The model size depends on the weights and bias in the hidden layers, so we controlled the network parameters by adjusting the numbers of nodes and layers. Table 2 shows 35 network architectures that were established for the prediction of optical properties. The total parameters of every network range from 10^2 to 10^6, and the model file sizes range from 25 kB to 10^4 kB.

To assess the performance of the networks, we used the coefficient of determination R^2 to evaluate the fitness between predictions and true values. The coefficient of determination is defined as follows:

$$R^2 = 1 - \frac{\sum_{i=1}^{M}(y_i - f_i)^2}{\sum_{i=1}^{M}(y_i - \bar{y})^2}\,, \tag{8}$$

$\bar{y}$ is the average of all true values.The closer R^2 is to 1, the higher the performance of the network is.

We tested all of the established models, and Fig. 2 shows the RMSE and R^2 of each network. The test data was fixed to 100 000 sets, which were chosen randomly from the testing dataset. The figure shows that the RMSE and R^2 from the testing sets reached a limit when the network parameters increased. The DNN models attained appreciable performance for predicting SSA, and g when the network parameters were of the order 10^4 to 10^5. At the same time, performance was optimized for P_{11} when the parameters were of

Table 2. Network structures that are established for the prediction of optical properties. The number of network parameters ranges from ~10^2 to ~10^6, and the model file size ranges from 25 KB to ~10^4 KB.

The nodes of layers	Total network parameters	Model file size (KB)
5, 16, 1	113	25
5, 32, 1	225	27
5, 64, 1	449	29
5, 8, 8, 1	129	32
5, 128, 1	897	35
5, 16, 16, 1	385	36
5, 16, 16, 16, 1	657	45
5, 32, 32, 1	1281	46
5, 256, 1	1793	47
5, 16, 16, 16, 16, 1	929	55
5, 64, 32, 1	2497	61
5, 32, 32, 32, 1	2337	66
5, 32, 32, 32, 32, 1	3393	84
5, 64, 64, 1	4609	86
5, 64, 64, 16, 1	5601	103
5, 64, 64, 32, 1	6657	116
5, 32, 32, 32, 32, 32, 1	5505	124
5, 128, 64, 1	9089	139
5, 64, 64, 64, 1	8769	142
5, 128, 64, 64, 1	13249	193
5, 128, 128, 1	17409	236
5, 64, 128, 64, 64, 1	21185	294
5, 128, 128, 64, 1	25601	338
5, 128, 128, 128, 1	33921	436
5, 64, 128, 128, 128, 64, 1	50049	640
5, 128, 256, 128, 1	66817	821
5, 256, 256, 128, 1	100353	1215
5, 128, 256, 256, 128, 1	132609	1600
5, 256, 256, 256, 1	133377	1602
5, 256, 256, 256, 256,1	199169	2380
5, 256, 256, 256, 256, 128, 1	231937	2771
5, 256, 256, 256, 256, 256, 1	264961	3159
5, 256, 256, 256, 256, 256, 256, 1	330753	3936
5, 128, 256, 256, 256, 256, 256, 256, 256, 256, 128, 1	527361	6272
5, 256, 256, 256, 256, 256, 512, 512, 256, 256, 256, 256, 256, 1	1053697	12456

the order 10^5 to 10^6. Benefits were no longer realized with further increases in the number of total parameters. In the testing process, we paid more attention to the total number of network parameters and did not specifically consider the influence of hidden layers and nodes of each layer on the network.

To replace the database with an optimized DNN model, we must consider both the model's file size and accuracy. Therefore, we chose a DNN model with minimal network parameters for each optical property and ensured that R^2 is greater than 0.999. The optimal model's storage size was different for the various optical properties. The size of the DNN files was 193 KB for Q_{ext}, 142 KB for SSA, 294 KB for g, and 3159 KB for the phase matrix elements P_{ij}. The architecture of selected networks is illustrated in Fig. 3.

3.2. *Performance of the DNN models*

To verify the optimized DNN model, we evaluated its performance in optical property prediction. We trained the DNN for target particle optical properties separately, as described in section 2.4. The verification was done with testing on 1) 100 000 sets that were chosen from the testing dataset randomly and 2) specific particles for which the optical properties are available or unavailable in the database. First, we randomly chose many discrete points from the testing dataset and then examined the fitness between the DNN predictions and the true values. This procedure can give a general picture of the model's overall performance. The number of data points is 100 000 for each optical property.

In Fig. 4, the top row shows that the R^2 values of Q_{ext}, SSA, and g, are 0.99991, 0.99988, and 0.99985, and the RMSEs are 0.0091, 0.0024, and 0.0029, respectively. The performance of the optimized models for the phase matrix elements P_{ij} is also illustrated in the remaining two rows in Fig. 4. The coefficient of determination, R^2, is greater than

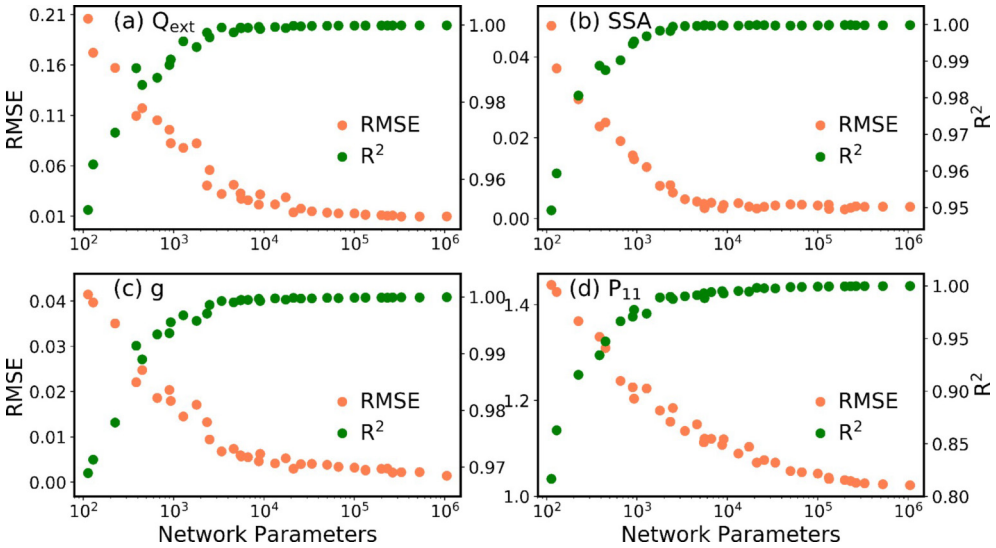

Fig. 2. Scatter plot of RMSE (orange dots) and the coefficient of determination R^2 (green dots) from several established DNN models for (a) Q_{ext}, (b) SSA, (c) g, and (d) P_{11}. In each subfigure, the left y-axis represents the RMSE, and the right y-axis represents R^2. As the network parameters increase, the DNN models have an upper limit of the prediction accuracy for each optical property.

Dense_1_Input: InputLayer	input:	$[(Q_{ext}, 5)]$	$[(SSA, 5)]$	$[(g, 5)]$	$[(P_{ij}, 6)]$
	output:	$[(Q_{ext}, 5)]$	$[(SSA, 5)]$	$[(g, 5)]$	$[(P_{ij}, 6)]$
Dense_1: Dense	input:	$(Q_{ext}, 5)$	$(SSA, 5)$	$(g, 5)$	$(P_{ij}, 6)$
	output:	$(Q_{ext}, 128)$	$(SSA, 64)$	$(g, 64)$	$(P_{ij}, 256)$
Dense_2: Dense	input:	$(Q_{ext}, 128)$	$(SSA, 64)$	$(g, 64)$	$(P_{ij}, 256)$
	output:	$(Q_{ext}, 64)$	$(SSA, 64)$	$(g, 128)$	$(P_{ij}, 256)$
Dense_3: Dense	input:	$(Q_{ext}, 64)$	$(SSA, 64)$	$(g, 128)$	$(P_{ij}, 256)$
	output:	$(Q_{ext}, 64)$	$(SSA, 64)$	$(g, 64)$	$(P_{ij}, 256)$
Dense_4: Dense	input:	$(Q_{ext}, 64)$	$(SSA, 64)$	$(g, 64)$	$(P_{ij}, 256)$
	output:	$(Q_{ext}, 1)$	$(SSA, 1)$	$(g, 64)$	$(P_{ij}, 256)$
Dense_5: Dense	input:	$(g, 64)$	$(P_{ij}, 256)$		
	output:	$(g, 1)$	$(P_{ij}, 256)$		
Dense_6: Dense	input:	$(P_{ij}, 256)$			
	output:	$(P_{ij}, 1)$			

Fig. 3. Deep Neural Network (DNN) architectures for Q_{ext}, SSA, g, and P_{ij}. The number of layers is 5, 5, 6, and 7 for Q_{ext}, SSA, g, and P_{ij}, respectively. The number of neuron nodes in the layer is included in the parentheses. For example, (Q_{ext}, 128) indicates 128 neuron nodes in a layer for the prediction of Q_{ext}.

0.999 for the phase function P_{11} and 0.99 for the other phase matrix elements. Therefore, the chosen DNN model has good learning capability. The original large database can be compressed into several small neural network models without losing much accuracy, and the compression ratio is approximately 6810 (from 133 377 877 kB to 19 583 kB).

Next, we compared the optical properties predicted from the DNN and the database values. Figure 5 shows the absolute errors of Q_{ext} calculated by the neural network and the database values. The results for SSA and g are shown in Figs. 6 and 7, respectively. Figures 5–7 present a broad picture of the model performance in reproducing the optical properties for particles available in the database. By identifying the upper and lower limits of errors, we can assess the model's ability to predict optical properties.

Table 3 lists the particle parameters chosen from the lighter colored areas (smaller errors) and darker colored areas (larger errors) in Figs. 5–7 to better understand the model's accuracy. Figures 8 (a–c) shows Q_{ext}, SSA, and g as functions of the size and shape parameters chosen from the lighter (smaller error) regions. The DNN and IITM results match almost perfectly, and the mean absolute errors (MAEs) are 0.003456, 0.001317, and 0.000876 for Q_{ext}, SSA, and g, respectively.

The lower panels of Figs. 8 (d–f) are similar to the upper panels but show the results from the darker (larger error) regions, including the darkest dot. The MAEs for Q_{ext}, SSA, and g are 0.006313, 0.001523, and 0.000945, respectively. Although relatively large errors were identified in darker regions, the predicted curves are still extremely consistent with the true values. The performance shown in Figs. 5–8 indicates that the DNN models can accurately calculate the optical properties of the particles contained in the whole database.

Next, we examined the learning capability of the selected DL scheme for cases with some parameters that are not in the datasets. Such an examination shows the robustness of the models by using what it has already learned to predict a new situation. In the database (as shown in Table 1), the real part of the refractive index m_{r} has values of 1.30 to 1.80

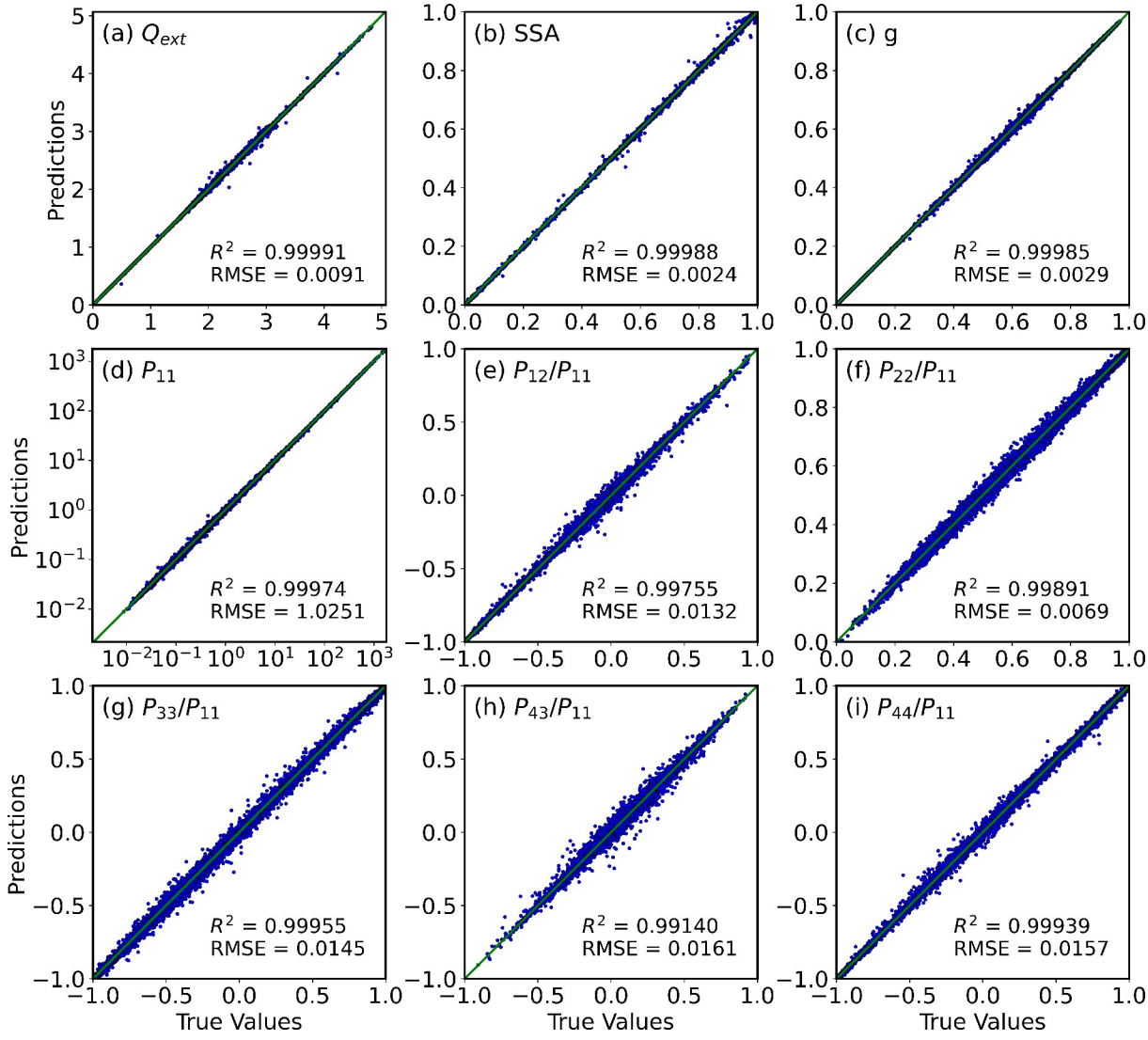

Fig. 4. Scatter plot of (a) Q_{ext}, (b) SSA, (c) g, (d) P_{11}, and (e) – (i) P_{ij}/P_{11} by DNN predictions against the true values.

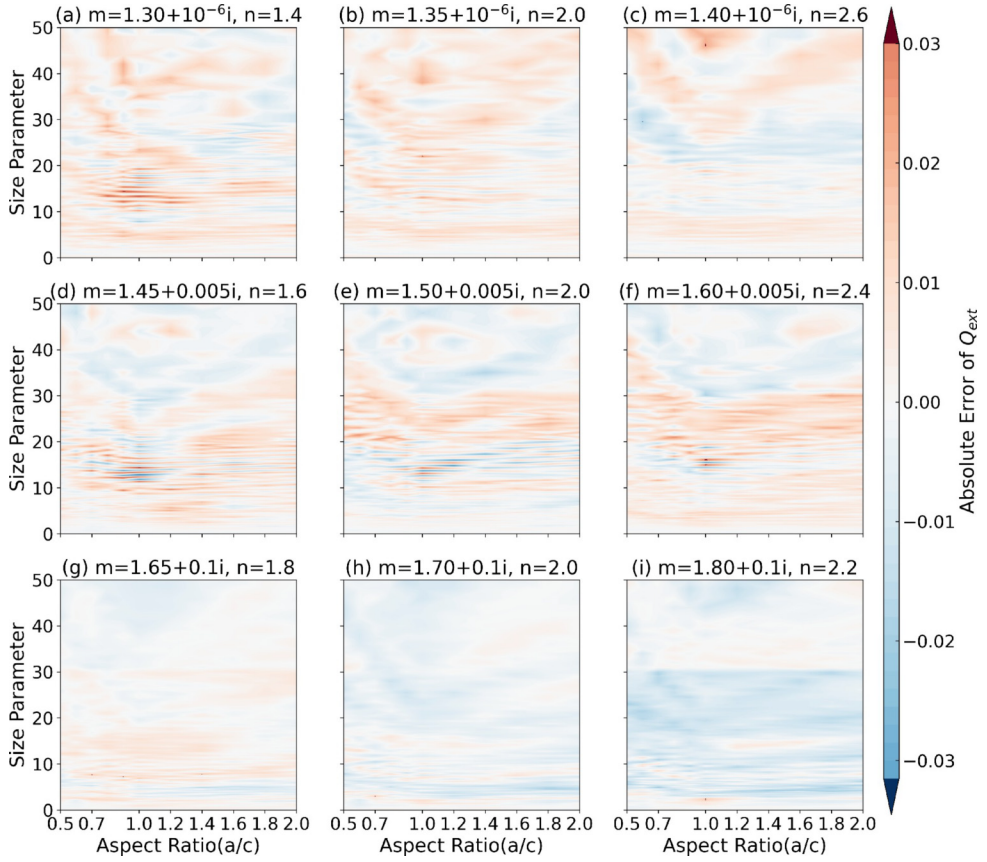

Fig. 5. Absolute errors of Q_{ext} predicted by the DNNs and the true values from the database.

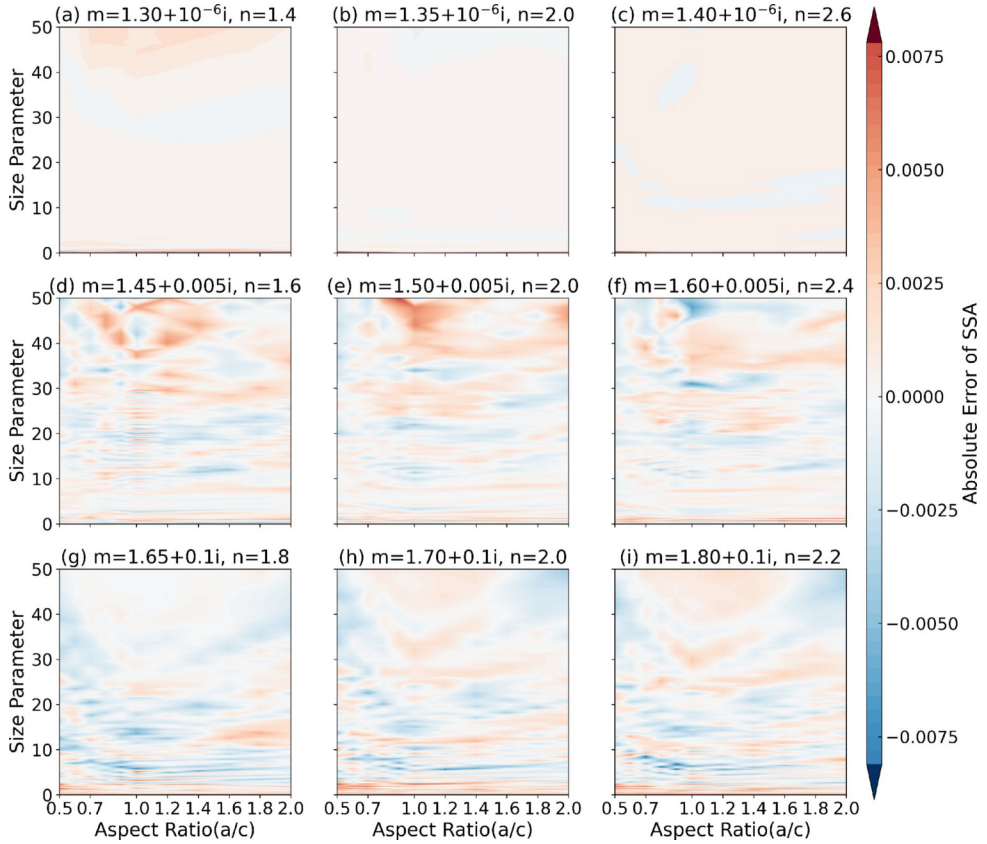

Fig. 6. Absolute errors of SSA predicted by the DNNs and the true values from the database.

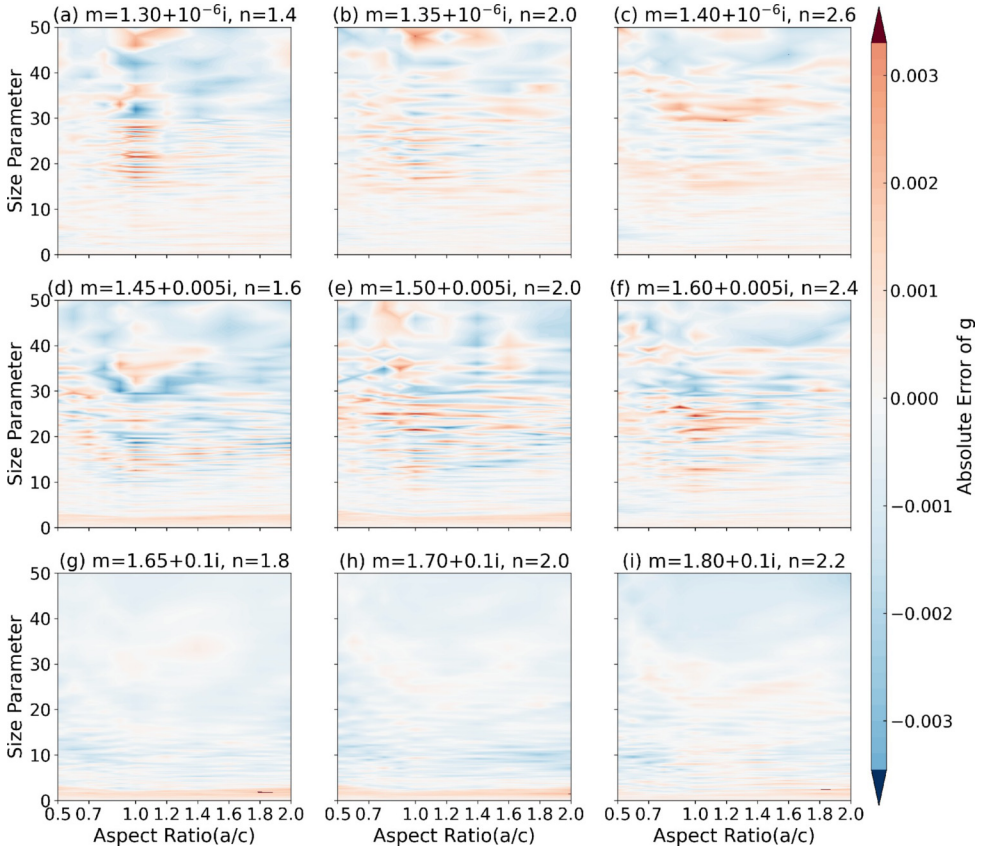

Fig. 7. Absolute errors of g predicted by the DNNs and the true values from the database.

Table 3. The test parameters of particles within the database. The particle parameters are chosen from the lighter colored areas and darker colored areas in Figs. 5, 6, and 7.

Optical properties	Particle parameters of lighter regions	Particle parameters of darker regions
Q_{ext}	m_r=1.40, m_i=10^{-6}, a/c =1.2, and n=2.6	m_r=1.30, m_i=10^{-6}, a/c =0.9, and n=1.4
SSA	m_r=1.70, m_i=0.1, a/c =1.8, and n=2.0	m_r=1.50, m_i=0.005, a/c =1.0, and n=2.0
g	m_r=1.45, m_i=0.005, a/c =1.6, and n=1.6	m_r=1.60, m_i=0.005, a/c =1.0, and n=2.4

with a step size of 0.05, the imaginary part of the refractive index m_i has values above 0.001 to 0.01 with a step size of 0.005 or 0.05. The size parameter xsize has integer values of 20 to 50 with a step size of 1. The unknown particle parameters that we tested are listed in Table 4.

To examine the accuracy of the predicted optical properties from the DNN, we also used the IITM to calculate the optical properties of these particles as reference values. The phase matrix element P_{ij}/P_{11} oscillates with respect to the scattering angle (P_{12}/P_{11} and P_{43}/P_{11} in particular). Nevertheless, a good agreement can still be obtained between the DNN and IITM results for all phase matrix elements. The numerical errors are expected to be further reduced if a bulk-scattering matrix is computed.

Figure 9 shows a comparison of the DNN prediction and the IITM results for case 1. The real part of the refractive index m_r is 1.45, the imaginary part m_i is 10^{-6}, the aspect ratio a/c is 0.6, the roundness parameter n is 2.4, and the size parameter xsize is 29.5. Yet again, there is excellent agreement between the DNNs and IITM, suggesting that the selected DL scheme is capable of predicting patterns given the values of parameters in the interpolation region. The most encouraging part is the remarkable increase in computing speed. Consider that when the size parameter (xsize) is fixed at 29.5, our models calculate all phase matrix elements in near-real-time (the average time is 1.2674 seconds), duly noting that the cost is more than 5 minutes if applying IITM to calculate them, especially if 24 central processing units are used.

Figure 10 shows the results for case 2, where the refractive index is also not in the training or testing grids (both the real part m_r and imaginary part m_i). In this computation, the real part of the refractive index m_r is 1.33, the imaginary part is 0.008, the aspect ratio a/c is 0.6, the roundness parameter n is 2.4, and the size parameter xsize is 38. These results imply that DNN models can predict the properties of a particle when the refractive index is not included in the database. Therefore, we can conclude that the DL scheme not only can significantly compress the whole database but it can also compute the optical properties of super-spheroids with

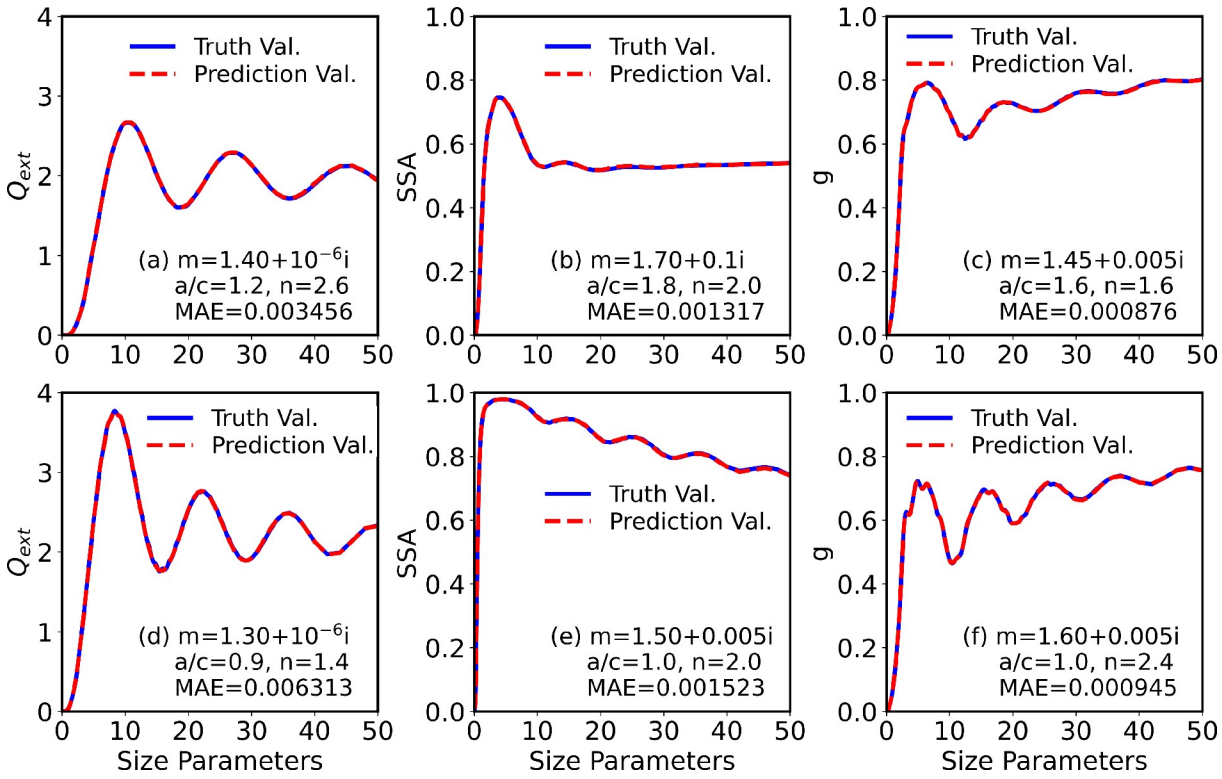

Fig. 8. Comparison of Q_{ext}, SSA, and g predicted by the DNNs against the true values in the database. The upper row (a–c) in the figure shows the results for parameters in light-colored areas, and the lower row (d–f) shows the results for parameters in dark-colored areas (Figs. 5–7). The mean absolute errors (MAEs) are also included in each subplot.

Table 4. The test parameters of unavailable particles in the database. In case 1, the size parameter xsize is fixed at 29.5. In case 2, the real part of the refractive index m_r is fixed at 1.33, and the imaginary part m_i is 0.008, and both of them are unavailable in the database. Case 3 is a "triple interpolation" scheme, and m_r, m_i, and xsize are not contained in the database.

	Particle parameters	Optical properties
Case 1	m_r=1.45, m_i=10^{-6}, a/c=0.6, n=2.4, and xsize=29.5	P_{11}, P_{12}/P_{11}, P_{22}/P_{11}, P_{33}/P_{11}, P_{43}/P_{11}, and P_{44}/P_{11}
Case 2	m_r=1.33, m_i=0.008, a/c =0.6, and n=2.4, and xsize=38	P_{11}, P_{12}/P_{11}, P_{22}/P_{11}, P_{33}/P_{11}, P_{43}/P_{11}, and P_{44}/P_{11}
Case 3	m_r=1.33, m_i=0.008, a/c =0.6, and n=2.4, and xsize=29.5	P_{11}, P_{12}/P_{11}, P_{22}/P_{11}, P_{33}/P_{11}, P_{43}/P_{11}, and P_{44}/P_{11}

reasonable accuracy for parameters that are not covered by the database.

Case 3 represents a "triple interpolation" scheme (for m_r, m_i, and xsize). In this case, the real part of the refractive index m_r is 1.33, the imaginary part is 0.008, the aspect ratio a/c is 0.6, the roundness parameter n is 2.4, and the size parameter xsize is 29.5. The results are shown in Fig. 11. Good agreement can still be obtained between the DNN and IITM results, even when three inputs of parameters are not available in the dataset. This finding indicates that the DNN models are able to predict the particle optical properties with reasonable accuracy. Furthermore, it is unnecessary to increase the resolution of parameters in the database.

4. Conclusion

We have successfully developed a DL approach to replace the direct use of a database of optical properties by using the super-spheroidal shape model. By constantly changing the architecture of the DNN, we identified several optimized models that have few parameters but, at the same time, achieved high accuracy. The selected DNNs demonstrated great capability in learning the optical properties relatively quickly with a coefficient of determination R^2> 0.999 from a sufficiently large dataset of 100,000 points randomly chosen from the testing dataset.

The database was compressed by a factor of 6810, and excellent accuracy was achieved, demonstrating the potential of obtaining accurate and real-time computation of optical properties. Truly impressive is the ability to capture the large oscillations of the phase matrix as the scattering angle changes. Even when the particle parameters are unavailable in the database, the DNNs are robust enough to obtain the optical properties of the particles with reasonable accuracy. Therefore, the DL scheme can reproduce the original database and predict the optical properties with unknown shape and refractive index parameters. Because of its small storage size and portability, the DNN model can be easily

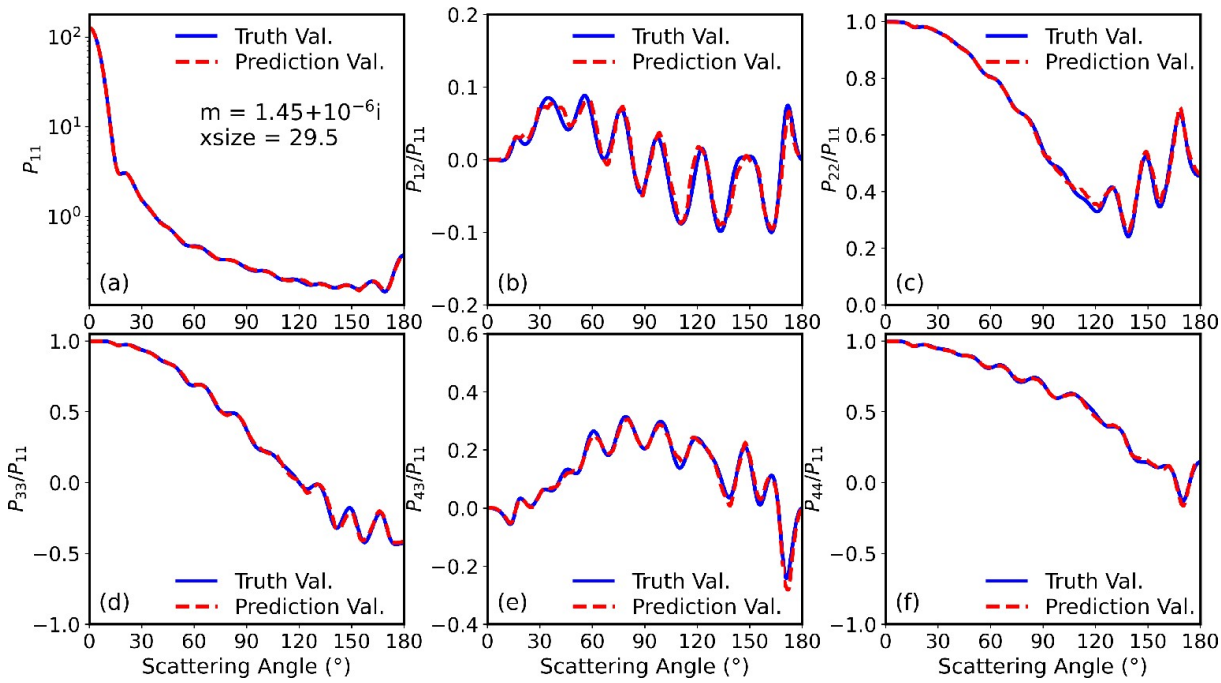

Fig. 9. Comparison of (a) P_{11}, (b) P_{12}/P_{11}, (c) P_{22}/P_{11}, (d) P_{33}/P_{11}, (e) P_{43}/P_{11}, and (f) P_{44}/P_{11} predicted by the DNNs against the true values. The size parameter xsize is unavailable in the database.

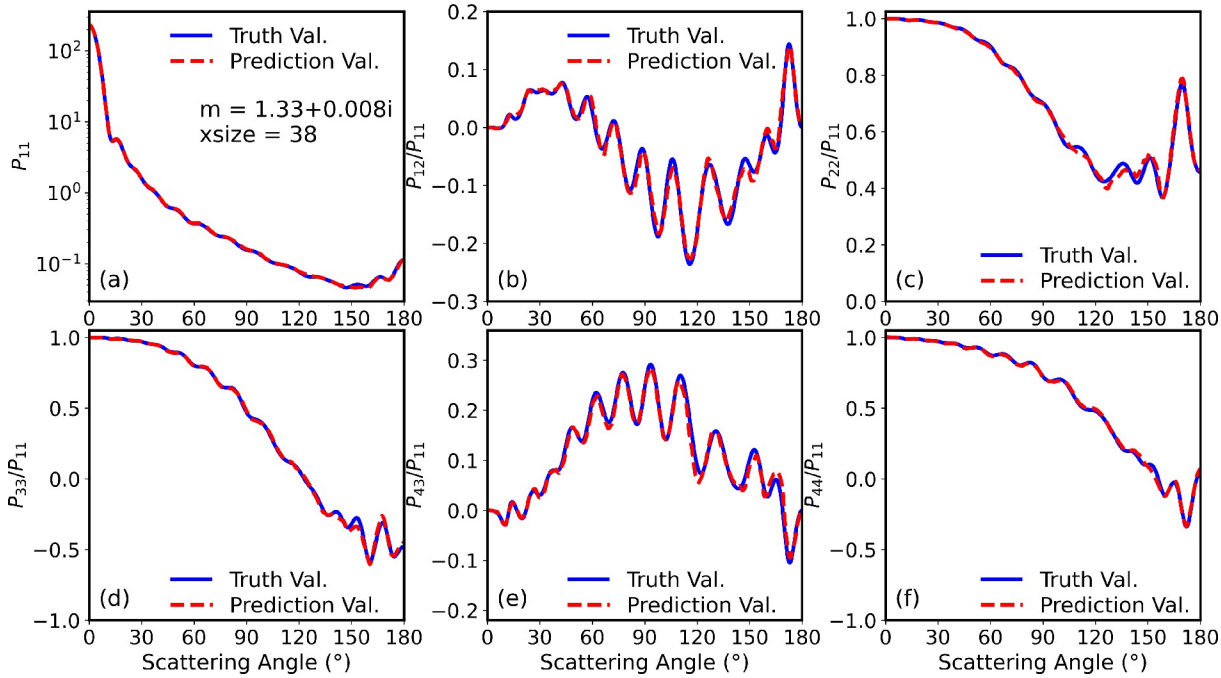

Fig. 10. Comparison of (a) P_{11}, (b) P_{12}/P_{11}, (c) P_{22}/P_{11}, (d) P_{33}/P_{11}, (e) P_{43}/P_{11}, and (f) P_{44}/P_{11} predicted from the DNNs against the true values. The refractive index is unavailable in the database.

applied to atmospheric radiative transfer, remote sensing inversion algorithms, or global climate simulations. However, it should be noted that the DNN model is not a physical light scattering model, but a convenient approach to parameterize the optical properties of particles. Because irregular, non-spherical particles can be reasonably approximated by the super-spheroidal shape (Bi et al., 2018; Lin et al., 2018; Sun et al., 2021), the DNN model developed in this study is expected to be quite useful in aerosol optics modeling. In future work, we will implement the DL scheme and DNN models into the Global/Regional Assimilation and Prediction Enhanced System (GRAPES) (Chen et al., 2008; Xue et al., 2008) and the Chinese Unified Atmospheric Chemistry Environment (CUACE) systems (Gong and Zhang, 2008; Zhou

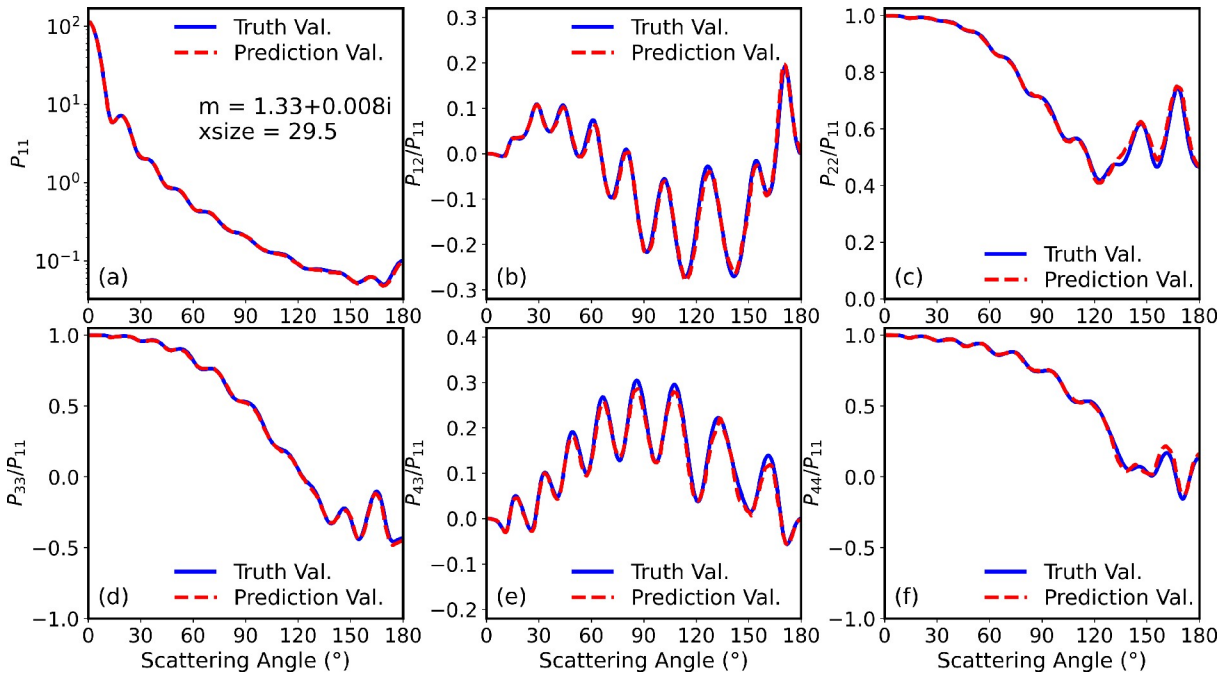

Fig. 11. Comparison of (a) P_{11}, (b) P_{12}/P_{11}, (c) P_{22}/P_{11}, (d) P_{33}/P_{11}, (e) P_{43}/P_{11}, and (f) P_{44}/P_{11} predicted from the DNNs against the true values. Both the size parameter xsize and refractive index are unavailable in the database.

et al., 2008, 2012, 2016; Wang et al., 2015, 2018).

Acknowledgements. We acknowledge Ms. Rui LIU from the Training Center of Atmospheric Sciences of Zhejiang University for her efforts managing computing resources and Dr. Wushao LIN for organizing the II-TM optical properties. A portion of the computations was performed in the National Supercomputer Center in Guangzhou (NSCC-GZ), Tianjin (NSCC-TJ), and Wuxi (NSCC-WX), as well as the cluster at State Key Lab of CAD&CG at Zhejiang University. This research was supported by the NSFC Major Project (Grant Nos. 42090030, and 42090032), the National Natural Science Foundation of China (Grant Nos. 42022038, and 42075155), and the National Key Research and Development Program (2019YFC1510400).

REFERENCES

Abadi, M., and Coauthors, 2016: TensorFlow: A system for large-scale machine learning. *Proc. 12th USENIX Symp. on Operating Systems Design and Implementation*, Savannah, USENIX, 265–283.

Barr, A. H., 1981: Superquadrics and angle-preserving transformations. *IEEE Computer Graphics and Applications*, **1**, 11–23, https://doi.org/10.1109/MCG.1981.1673799.

Bengio, Y., 2009: Learning deep architectures for AI. *Foundations and Trends® in Machine Learning*, **2**, 1–127, https://doi.org/10.1561/2200000006.

Bi, L., and P. Yang, 2014: Accurate simulation of the optical properties of atmospheric ice crystals with the invariant imbedding T-matrix method. *Journal of Quantitative Spectroscopy and Radiative Transfer*, **138**, 17–35, https://doi.org/10.1016/j.jqsrt.2014.01.013.

Bi, L., and P. Yang, 2017: Improved ice particle optical property simulations in the ultraviolet to far-infrared regime. *Journal of Quantitative Spectroscopy and Radiative Transfer*, **189**, 228–237, https://doi.org/10.1016/j.jqsrt.2016.12.007.

Bi, L., P. Yang, G. W. Kattawar, and R. Kahn, 2009: Single-scattering properties of triaxial ellipsoidal particles for a size parameter range from the Rayleigh to geometric-optics regimes. *Appl. Opt.*, **48**, 114–126, https://doi.org/10.1364/AO.48.000114.

Bi, L., P. Yang, G. W. Kattawar, and M. I. Mishchenko, 2013a: A numerical combination of extended boundary condition method and invariant imbedding method applied to light scattering by large spheroids and cylinders. *Journal of Quantitative Spectroscopy and Radiative Transfer*, **123**, 17–22, https://doi.org/10.1016/j.jqsrt.2012.11.033.

Bi, L., P. Yang, G. W. Kattawar, and M. I. Mishchenko, 2013b: Efficient implementation of the invariant imbedding T-matrix method and the separation of variables method applied to large non-spherical inhomogeneous particles. *Journal of Quantitative Spectroscopy and Radiative Transfer*, **116**, 169–183, https://doi.org/10.1016/j.jqsrt.2012.11.014.

Bi, L., W. S. Lin, Z. Wang, X. Y. Tang, X. Y. Zhang, and B. Q.

Yi, 2018: Optical modeling of sea salt aerosols: The effects of nonsphericity and inhomogeneity. *J. Geophys. Res. Atmos.*, **123**, 543–558, https://doi.org/10.1002/2017JD027869.

Bohren, C. F., and D. R. Huffman, 1983: *Absorption and Scattering of Light by Small Particles*. Wiley, 530 pp.

Charlson, R. J., S. E. Schwartz, J. M. Hales, R. D. Cess, J. A. Coakley Jr., J. E. Hansen, and D. J. Hofmann, 1992: Climate forcing by anthropogenic aerosols. *Science*, **255**, 423–430, https://doi.org/10.1126/science.255.5043.423.

Chen, D. H., and Coauthors, 2008: New generation of multi-scale NWP system (GRAPES): General scientific design. *Chinese Science Bulletin*, **53**, 3433–3445, https://doi.org/10.1007/s11434-008-0494-z.

Chen, Y. S., H. L. Jiang, C. Y. Li, X. P. Jia, and P. Ghamisi, 2016: Deep feature extraction and classification of hyperspectral images based on convolutional neural networks. *IEEE Trans. Geosci. Remote Sens.*, **54**, 6232–6251, https://doi.org/10.1109/TGRS.2016.2584107.

Di Noia, A., and O. P. Hasekamp, 2018: Neural networks and support vector machines and their application to aerosol and cloud remote sensing: A review. *Springer Series in Light Scattering*: *Volume 1*: *Multiple Light Scattering*, *Radiative Transfer and Remote Sensing*, A. Kokhanovsky, Ed., Springer, 279–329, https://doi.org/10.1007/978-3-319-70796-9_4.

Draine, B. T., and P. J. Flatau, 1994: Discrete-dipole approximation for scattering calculations. *Journal of the Optical Society of America A*, **11**, 1491–1499, https://doi.org/10.1364/JOSAA.11.001491.

Dubovik, O., B. Holben, T. F. Eck, A. Smirnov, Y. J. Kaufman, M. D. King, D. Tanré, and I. Slutsker, 2002: Variability of absorption and optical properties of key aerosol types observed in worldwide locations. *J. Atmos. Sci.*, **59**, 590–608, https://doi.org/10.1175/1520-0469(2002)059<0590:VOAAOP>2.0.CO;2.

Dubovik, O., and Coauthors, 2006: Application of spheroid models to account for aerosol particle nonsphericity in remote sensing of desert dust. *J. Geophys. Res. Atmos.*, **111**, D11208, https://doi.org/10.1029/2005JD006619.

Dubovik, O., T. Lapyonok, Y. J. Kaufman, M. Chin, P. Ginoux, R. A. Kahn, and A. Sinyuk, 2008: Retrieving global aerosol sources from satellites using inverse modeling. *Atmospheric Chemistry and Physics*, **8**, 209–250, https://doi.org/10.5194/acp-8-209-2008.

Dubovik, O., and Coauthors, 2019: Polarimetric remote sensing of atmospheric aerosols: Instruments, methodologies, results, and perspectives. *Journal of Quantitative Spectroscopy and Radiative Transfer*, **224**, 474–511, https://doi.org/10.1016/j.jqsrt.2018.11.024.

Glorot, X., and Y. Bengio, 2010: Understanding the difficulty of training deep feedforward neural networks. *Proc. 13th Int. Conf. on Artificial Intelligence and Statistics (AISTATS) 2010*, Sardinia, JMLR, 249–256.

Glorot, X., A. Bordes, and Y. Bengio, 2011: Deep sparse rectifier neural networks. *Proc. Fourteenth Int. Conf. on Artificial Intelligence and Statistics*, Fort Lauderdale, PMLR, 315–323.

Gong, S. L., and X. Y. Zhang, 2008: CUACE/Dust-an integrated system of observation and modeling systems for operational dust forecasting in Asia. *Atmospheric Chemistry and Physics*, **8**, 2333–2340, https://doi.org/10.5194/acp-8-2333-2008.

Groth, S. P., A. J. Baran, T. Betcke, S. Havemann, and W. Śmigaj, 2015: The boundary element method for light scattering by ice crystals and its implementation in BEM++. *Journal of Quantitative Spectroscopy and Radiative Transfer*, **167**, 40–52, https://doi.org/10.1016/j.jqsrt.2015.08.001.

Ham, Y. G., J. H. Kim, and J. J. Luo, 2019: Deep learning for multi-year ENSO forecasts. *Nature*, **573**, 568–572, https://doi.org/10.1038/s41586-019-1559-7.

Heintzenberg, J., and Coauthors, 1997: Measurements and modelling of aerosol single-scattering albedo: Progress, problems and prospects. *Contrib. Atmos. Phys.*, **70**, 249–263.

Hinton, G., and Coauthors, 2012: Deep neural networks for acoustic modeling in speech recognition: The shared views of four research groups. *IEEE Signal Processing Magazine*, **29**, 82–97, https://doi.org/10.1109/MSP.2012.2205597.

Hinton, G. E., and R. R. Salakhutdinov, 2006: Reducing the dimensionality of data with neural networks. *Science*, **313**, 504–507, https://doi.org/10.1126/science.1127647.

IPCC, 2013: *Climate Change 2013*: *The Physical Science Basis*. *Contribution of Working Group I to the Fifth Assessment Report of the Intergovernmental Panel on Climate*. Cambridge University Press, 1535 pp.

Johnson, B. R., 1988: Invariant imbedding T matrix approach to electromagnetic scattering. *Appl. Opt.*, **27**, 4861–4873, https://doi.org/10.1364/AO.27.004861.

Kahnert, F. M., J. J. Stamnes, and K. Stamnes, 2002: Using simple particle shapes to model the Stokes scattering matrix of ensembles of wavelength-sized particles with complex shapes: Possibilities and limitations. *Journal of Quantitative Spectroscopy and Radiative Transfer*, **74**, 167–182, https://doi.org/10.1016/S0022-4073(01)00194-7.

Kahnert, M., A. Kylling, 2004: Radiance and flux simulations for mineral dust aerosols: Assessing the error due to using spherical or spheroidal model particles. *J. Geophys. Res. Atmos.*, **109**, D09203, https://doi.org/10.1029/2003JD004318.

Kahnert, M., T. Nousiainen, and P. Räisänen, 2007: Mie simulations as an error source in mineral aerosol radiative forcing calculations. *Quart. J. Roy. Meteor. Soc.*, **133**, 299–307, https://doi.org/10.1002/qj.40.

Kahnert, M., T. Nousiainen, and H. Lindqvist, 2014: Review: Model particles in atmospheric optics. *Journal of Quantitative Spectroscopy and Radiative Transfer*, **146**, 41–58, https://doi.org/10.1016/j.jqsrt.2014.02.014.

King, M. D., Y. J. Kaufman, D. Tanré, and T. Nakajima, 1999: Remote sensing of tropospheric aerosols from space: Past, present, and future. *Bull. Amer. Meteor Soc.*, **80**, 2229–2260, https://doi.org/10.1175/1520-0477(1999)080<2229:RSOTAF>2.0.CO;2.

Kingma, D. P., and L. J. Ba, 2015: Adam: A method for stochastic optimization. *Proc. 3rd International Conf. on Learning Representations*, San Diego, ICLR.

Kok, J. F., and Coauthors, 2017: Integrative analysis of desert dust size and abundance suggests less dust climate cooling. *Nature Geoscience*, **10**, 274–278, https://doi.org/10.1038/ngeo2912.

Krizhevsky, A., I. Sutskever, and G. E. Hinton, 2012: ImageNet classification with deep convolutional neural networks. *Proc. 25th Int. Conf. on Neural Information Processing Systems*, Lake Tahoe, ACM, 1097–1105, https://doi.org/10.5555/2999134.2999257.

LeCun, Y., Y. Bengio, and G. Hinton, 2015: Deep learning. *Nature*, **521**, 436–444, https://doi.org/10.1038/nature14539.

Li, Z., F. Niu, J. W. Fan, Y. J. Liu, D. Rosenfeld, and Y. N. Ding,

2011: Long-term impacts of aerosols on the vertical development of clouds and precipitation. *Nature Geoscience*, **4**, 888–894, https://doi.org/10.1038/ngeo1313.

Lin, W. S., L. Bi, and O. Dubovik, 2018: Assessing superspheroids in modeling the scattering matrices of dust aerosols. *J. Geophys. Res. Atmos.*, **123**, 13 917–13 943, https://doi.org/10.1029/2018JD029464.

Liu, C., R. Lee Panetta, and P. Yang, 2012: Application of the pseudo-spectral time domain method to compute particle single-scattering properties for size parameters up to 200. *Journal of Quantitative Spectroscopy and Radiative Transfer*, **113**, 1728–1740, https://doi.org/10.1016/j.jqsrt.2012.04.021.

Liu, Q. H., 1997: The PSTD algorithm: A time-domain method requiring only two cells per wavelength. *Microwave and Optical Technology Letters*, **15**, 158–165, https://doi.org/10.1002/(SICI)1098-2760(19970620)15:3<158::AID-MOP11>3.0.CO;2-3.

Mishchenko, M. I., and M. A. Yurkin, 2017: On the concept of random orientation in far-field electromagnetic scattering by non-spherical particles. *Opt. Lett.*, **42**, 494–497, https://doi.org/10.1364/OL.42.000494.

Mishchenko, M. I., A. A. Lacis, B. E. Carlson, and L. D. Travis, 1995: Nonsphericity of dust-like tropospheric aerosols: Implications for aerosol remote sensing and climate modeling. *Geophys. Res. Lett.*, **22**, 1077–1080, https://doi.org/10.1029/95GL00798.

Mishchenko, M. I., and Coauthors, 2003: Aerosol retrievals from AVHRR radiances: Effects of particle nonsphericity and absorption and an updated long-term global climatology of aerosol properties. *Journal of Quantitative Spectroscopy and Radiative Transfer*, **79–80**, 953–972, https://doi.org/10.1016/S0022-4073(02)00331-X.

Morman, S. A., and G. S. Plumlee, 2013: The role of airborne mineral dusts in human disease. *Aeolian Research*, **9**, 203–212, https://doi.org/10.1016/j.aeolia.2012.12.001.

Myhre, G., and Coauthors, 2013: Anthropogenic and Natural Radiative Forcing. *Climate Change 2013: The Physical Science Basis. Contribution of Working Group I to the Fifth Assessment Report of the Intergovernmental Panel on Climate Change. Cambridge University Press*, 659–740.

Nousiainen, T., M. Kahnert, and H. Lindqvist, 2011: Can particle shape information be retrieved from light-scattering observations using spheroidal model particles. *Journal of Quantitative Spectroscopy and Radiative Transfer*, **112**, 2213–2225, https://doi.org/10.1016/j.jqsrt.2011.05.008.

Oquab, M., L. Bottou, I. Laptev, and J. Sivic, 2014: Learning and transferring mid-level image representations using convolutional neural networks. *Proc. 2014 IEEE Conference on Computer Vision and Pattern Recognition*, Columbus, IEEE, 1717–1724, https://doi.org/10.1109/CVPR.2014.222.

Rosenfeld, D., 2000: Suppression of rain and snow by urban and industrial air pollution. *Science*, **287**, 1793–1796, https://doi.org/10.1126/science.287.5459.1793.

Rosenfeld, D., U. Lohmann, G. B. Raga, C. D. O'dowd, M. Kulmala, S. Fuzzi, A. Reissell, and M. O. Andreae, 2008: Flood or drought: How do aerosols affect precipitation. *Science*, **321**, 1309–1313, https://doi.org/10.1126/science.1160606.

Saito, M., P. Yang, J. C. Ding, and X. Liu, 2021: A comprehensive database of the optical properties of irregular aerosol particles for radiative transfer simulations. *J. Atmos. Sci.*, **78**, 2089–2111, https://doi.org/10.1175/JAS-D-20-0338.1.

Satheesh, S. K., and K. K. Moorthy, 2005: Radiative effects of natural aerosols: A review. *Atmos. Environ.*, **39**, 2089–2110, https://doi.org/10.1016/j.atmosenv.2004.12.029.

Schmidhuber, J., 2017: Deep Learning. *Encyclopedia of Machine Learning and Data Mining*, C. Sammut and G. I. Webb, Eds., Springer, 338–348, https://doi.org/10.1007/978-1-4899-7502-7_909-1.

Shrivastava, A., A. Kundu, C. Dhir, D. Naik, and O. Tuzel, 2021: Optimize what matters: Training DNN-Hmm keyword spotting model using end metric. Preprints, ICASSP 2021–2021 IEEE International Conference on Acoustics, Speech and Signal Processing (ICASSP), Toronto, IEEE, 4000–4004, https://doi.org/10.1109/ICASSP39728.2021.9414797.

Silver, D., and Coauthors, 2016: Mastering the game of Go with deep neural networks and tree search. *Nature*, **529**, 484–489, https://doi.org/10.1038/nature16961.

Sokolik, I., A. Andronova, and T. C. Johnson, 1993: Complex refractive index of atmospheric dust aerosols. *Atmos. Environ. Part A Gene. Top.*, **27**, 2495–2502, https://doi.org/10.1016/0960-1686(93)90021-P.

Sun, L.-H., L. Bi, and B. Q. Yi, 2021: The use of superspheroids as surrogates for modeling electromagnetic wave scattering by ice crystals. *Remote Sensing*, **13**, 1733, https://doi.org/10.3390/rs13091733.

Tang, X. Y., L. Bi, W. S. Lin, D. Liu, K. J. Zhang, and W. J. Li, 2019: Backscattering ratios of soot-contaminated dusts at triple LiDAR wavelengths: T-matrix results. *Optics Express*, **27**, A92–A116, https://doi.org/10.1364/OE.27.000A92.

Tegen, I., A. A. Lacis, and I. Fung, 1996: The influence on climate forcing of mineral aerosols from disturbed soils. *Nature*, **380**, 419–422, https://doi.org/10.1038/380419a0.

Van De Hulst, H. C., 1981: *Light Scattering by Small Particles*. Dover, 485 pp.

Wang, G. H., and Coauthors, 2016: Persistent sulfate formation from London Fog to Chinese haze. *Proceedings of the National Academy of Sciences of the United States of America*, **113**, 13 630–13 635, https://doi.org/10.1073/pnas.1616540113.

Wang, H., G. Y. Shi, X. Y. Zhang, S. L. Gong, S. C. Tan, B. Chen, H. Z. Che, and T. Li, 2015: Mesoscale modelling study of the interactions between aerosols and PBL meteorology during a haze episode in China Jing–Jin–Ji and its near surrounding region–Part 2: Aerosols' radiative feedback effects. *Atmospheric Chemistry and Physics*, **15**, 3277–3287, https://doi.org/10.5194/acp-15-3277-2015.

Wang, H., Y. Peng, X. Y. Zhang, H. L. Liu, M. Zhang, H. Z. Che, Y. L. Cheng, and Y. Zheng, 2018: Contributions to the explosive growth of $PM_{2.5}$ mass due to aerosol–radiation feedback and decrease in turbulent diffusion during a red alert heavy haze in Beijing–Tianjin–Hebei, China. *Atmospheric Chemistry and Physics*, **18**, 17 717–17 733, https://doi.org/10.5194/acp-18-17717-2018.

Wang, Z., L. Bi, B. Q. Yi, and X. Y. Zhang, 2019: How the inhomogeneity of wet sea salt aerosols affects direct radiative forcing. *Geophys. Res. Lett.*, **46**, 1805–1813, https://doi.org/10.1029/2018GL081193.

Wriedt, T., 2002: Using the T-matrix method for light scattering computations by non-axisymmetric particles: Superellipsoids and realistically shaped particles. *Particle & Particle Systems Characterization*, **19**, 256–268, https://doi.org/10.1002/1521-4117(200208)19:4<256::AID-PPSC256>3.0.CO;2-8.

Xue, J. S., S. Y. Zhuang, G. F. Zhu, H. Zhang, Z. Q. Liu, Y. Liu, and Z. R. Zhuang, 2008: Scientific design and preliminary

results of three-dimensional variational data assimilation system of GRAPES. *Chinese Science Bulletin*, **53**, 3446–3457, https://doi.org/10.1007/s11434-008-0416-0.

Yang, P., and K. N. Liou, 1996a: Geometric-optics-integral-equation method for light scattering by non-spherical ice crystals. *Appl. Opt.*, **35**, 6568–6584, https://doi.org/10.1364/AO.35.006568.

Yang, P., and K. N. Liou, 1996b: Finite-difference time domain method for light scattering by small ice crystals in three-dimensional space. *Journal of the Optical Society of America A*, **13**, 2072–2085, https://doi.org/10.1364/JOSAA.13.002072.

Yang, P., and Coauthors, 2007: Modeling of the scattering and radiative properties of non-spherical dust-like aerosols. *Journal of Aerosol Science*, **38**, 995–1014, https://doi.org/10.1016/j.jaerosci.2007.07.001.

Yang, P., L. Bi, B. A. Baum, K.-N. Liou, G. W. Kattawar, M. I. Mishchenko, and B. Cole, 2013: Spectrally consistent scattering, absorption, and polarization properties of atmospheric ice crystals at wavelengths from 0.2 to 100 μm. *J. Atmos. Sci.*, **70**, 330–347, https://doi.org/10.1175/JAS-D-12-039.1.

Yee, K., 1966: Numerical solution of initial boundary value problems involving maxwell's equations in isotropic media. *IEEE Trans. Antennas Propag.*, **14**, 302–307, https://doi.org/10.1109/TAP.1966.1138693.

Yurkin, M. A., and A. G. Hoekstra, 2011: The discrete-dipole-approximation code ADDA: Capabilities and known limitations. *Journal of Quantitative Spectroscopy and Radiative Transfer*, **112**, 2234–2247, https://doi.org/10.1016/j.jqsrt.2011.01.031.

Zhang, R. Y., 2010: Getting to the critical nucleus of aerosol formation. *Science*, **328**, 1366–1367, https://doi.org/10.1126/science.1189732.

Zhang, X. Y., J. Z. Wang, Y. Q. Wang, H. L. Liu, J. Y. Sun, and Y. M. Zhang, 2015: Changes in chemical components of aerosol particles in different haze regions in China from 2006 to 2013 and contribution of meteorological factors. *Atmospheric Chemistry and Physics*, **15**, 12 935–12 952, https://doi.org/10.5194/acp-15-12935-2015.

Zhao, T. X.-P., I. Laszlo, O. Dubovik, B. N. Holben, J. Sapper, D. Tanré, and C. Pietras, 2003: A study of the effect of non-spherical dust particles on the AVHRR aerosol optical thickness retrievals. *Geophys. Res. Lett.*, **30**, 1317, https://doi.org/10.1029/2002GL016379.

Zhou, C., X. Zhang, S. Gong, Y. Wang, and M. Xue, 2016: Improving aerosol interaction with clouds and precipitation in a regional chemical weather modeling system. *Atmospheric Chemistry and Physics*, **16**, 145–160, https://doi.org/10.5194/acp-16-145-2016.

Zhou, C. H., and Coauthors, 2008: Development and evaluation of an operational SDS forecasting system for East Asia: CUACE/Dust. *Atmospheric Chemistry and Physics*, **8**, 787–798, https://doi.org/10.5194/acp-8-787-2008.

Zhou, C.-H., and Coauthors, 2012: Towards the improvements of simulating the chemical and optical properties of Chinese aerosols using an online coupled model–CUACE/Aero. *Tellus B: Chemical and Physical Meteorology*, **64**, 18965, https://doi.org/10.3402/tellusb.v64i0.18965.